fluids

MDPI

Article

Deeper Flow Behavior Explanation of Temperature Effects on the Fluid Dynamic inside a Tundish

Enif Gutiérrez [1], Saul Garcia-Hernandez [1,*], Rodolfo Morales Davila [2] and Jose de Jesus Barreto [1]

[1] Metallurgy Graduate Center, TecNM-Instituto Tecnologico de Morelia, Av. Tecnologico No. 1500, Morelia 58120, Mexico; enif.gg@morelia.tecnm.mx (E.G.); jose.bs@morelia.tecnm.mx (J.d.J.B.)
[2] Departament of Metallurgy and Materials Engineering-ESIQUIE, Instituto Politécnico Nacional, Ed. 7, UPALM, Col. Zacatenco, Ciudad de México 07738, Mexico; rmorales@ipn.mx
* Correspondence: saul.gh@morelia.tecnm.mx

Abstract: The continuous casting tundish is non-isothermal due to heat losses and temperature variation from the inlet stream, which generate relevant convection forces. This condition is commonly avoided through qualitative fluid dynamic analysis only. This work searches to establish the conditions for which non-isothermal simulations are mandatory or for which isothermal simulations are enough to accurately describe the fluid dynamics inside the tundish by quantifying the buoyant and inertial forces. The mathematical model, simulated by CFD software, considers the Navier-Stokes equations, the realizable k-ε model for solving the turbulence, and the Lagrangian discrete phase to track the inclusion trajectories. The results show that temperature does not significantly impact the volume fraction percentages or the mean residence time results; nevertheless, bigger velocity magnitudes under non-isothermal conditions than in isothermal conditions and noticeable changes in the fluid dynamics between isothermal and non-isothermal cases in all the zones where buoyancy forces dominate over inertial forces were observed. Because of the results, it is concluded that isothermal simulations can accurately describe the flow behavior in tundishes when the flow control devices control the fluid dynamics, but simulations without control devices or with a weak fluid dynamic dependence on the control devices require non-isothermal simulations.

Keywords: mathematical simulation; non-isothermal model; isothermal model; ideal volume fractions; inclusion removal rates

Citation: Gutiérrez, E.; Garcia-Hernandez, S.; Davila, R.M.; de Jesus Barreto, J. Deeper Flow Behavior Explanation of Temperature Effects on the Fluid Dynamic inside a Tundish. *Fluids* **2024**, *9*, 21. https://doi.org/10.3390/fluids9010021

Academic Editors: D. Andrew S. Rees and Francesco De Vanna

Received: 6 December 2023
Revised: 30 December 2023
Accepted: 5 January 2024
Published: 10 January 2024

1. Introduction

The tundish is an essential reactor of the continuous casting machine. Its primordial goal is to feed the mold with steel that is homogeneous in temperature and chemical composition. Additionally, the tundish tries to minimize the new inclusion generation and improve the inclusion removal, implying that its good operation guarantees high-quality steel production. Focusing on tundish temperature control, the slag layer on the tundish top provides thermal insulation to prevent the molten steel from losing heat to the atmosphere. However, heat losses exist throughout steel contact with the refractory walls, flow control devices, and even more from heat to heat. Because of that, in recent years, more researchers have considered the temperature variable in their simulations [1–26] versus most previous works, which ignore their effects [27–45]. Both approaches have generated debate about the importance of temperature on flow patterns among researchers [19–26]. Some assure that temperature effects strongly impact the flow patterns inside the tundish. For example, Miki et al. [19], studying a tundish with one strand and a dam, found a steel temperature drop of five grades inside the tundish, generating notorious changes in the fluid dynamics compared with the isothermal case due to the thermal convection, which also induces a stronger inclusion removal rate for the non-isothermal case. Alizadeth et al. [20], studying a tundish with two strands, a turbulence inhibitor, and dams, analyze the RTDs for isothermal and non-isothermal conditions, determining that the mixed fraction

volume is lower for the isothermal case than the non-isothermal case due to the buoyancy force forcing the flow towards the top surface. Sun et al. [21], studying a single-strand tundish with a turbulence inhibitor, dam, weir, and stopper rod, confirm the results reported by Alizadeth [20] and additionally note that the RTD-s for both cases have the same tendency, concluding that although the isothermal simulation cannot reflect in detail the flow patterns, they can determine the optimal design for the flow controls. Chaterjee et al. [22], studying a tundish with four strands and an impact pad, found that the flow patterns far from the inlet zone can change drastically in a non-isothermal case. The temperature induces a strong inclusion coupling with the flow, which induces an increment in the removal inclusion rate. Zhu et al. [23] use a four-strand tundish with baffles, finding that control devices can cushion but not eliminate the temperature impact.

In contrast, other researchers affirm that this variable is unimportant, disdaining the temperature effects for considering them insignificant. For example, Morales et al. [24], using a two-strand tundish with a weir, dam, and turbulence inhibitor, determined that the thermal disturbances due to the ladle change modify the fluid dynamics immediately after the input. Still, the flow behaves similarly to an isothermal state after a short period. Using a four-strand tundish, Chattopadhyay et al. [25] found a strong influence of the natural convection if the tundish is empty; however, using an impact pad, the temperature effects on the fluid dynamics and removal rates vanish. Sousa Rocha et al. [26], using a two-strand tundish with different configurations for the flow control devices, did not find substantial differences between the isothermal and non-isothermal cases.

The previously mentioned works studied and clarified the differences and similitudes between isothermal and non-isothermal simulations on the steel flow patterns in the tundish. Nevertheless, all these efforts are qualitative, and it is still undetermined if the temperature does or does not substantially affect the flow patterns and if the flow control devices can or cannot cancel out the temperature effects on the fluid dynamics. Therefore, this work aims to establish the conditions for which non-isothermal simulations are mandatory or for which isothermal simulations are enough to accurately describe the fluid dynamics inside the tundish by quantifying the buoyant and inertial forces. To achieve this, a mathematical model will be validated using a scaled water model to later employ the validated model to study the effect of temperature on fluid dynamics by flow pattern analysis and by quantifying the changes in the variation of the non-ideal flows inside the tundish.

2. Numerical Methods

The commercial ANSYS Fluent® CFD code (Fluent 16.0, Ansys Inc., Centerra Resource Park, Lebanon, 2009) solved the equations simultaneously using the following assumptions and considerations:

2.1. Main Assumptions and Considerations

Three Cartesian coordinates consider isothermal and non-isothermal conditions. The gravity force acts vertically in the incoming flow direction. The typical non-slip conditions apply to solid surfaces. The molten steel behaves as an incompressible Newtonian fluid. The simulation considers an air zone of 100 mm and a slag zone of 70 mm. The non-isothermal simulation considers a tundish wall of magnesia. The physical properties of steel, slag, air, and magnesia are in Table 1.

The inlet and outlet temperatures were 1800 K and 1793 K, respectively. Heat losses from the bottom, walls, and flow control devices are in Table 2. The inlet and outlet velocities were calculated based on the volumetric flow of 297.8 L/min.

The simulated inclusions were assumed to be of spherical, rigid shape and to have the physical properties of alumina (density = 3960 kg/m^3). No interaction among the inclusions was considered; therefore, agglomeration and collision were not simulated. The inclusion-removal mechanism considered was Stokes flotation. The boundary conditions for inclusion removal were as follows: any inclusion that reached the interphase slag-steel

was considered removed, and the rest was considered escaped. Inclusion trajectories were calculated using a Lagrangian particle-tracking approach, which solves a transport equation for each inclusion as they travel through the previously calculated velocity field of liquid steel. This approach assumes that the interaction between steel and the inclusion is one-way coupled; that is, only the steel affects the trajectories of inclusions, but these do not affect the steel flow. Once isothermal and non-isothermal cases achieve the quasi-steady state, 2000 inclusions of a single size 1, 20, 40, 60, 80, 100, 130, 150, 180, and 200 μm were fed as an impulse at the ladle shroud surface entry.

Table 1. Physical properties of steel, slag, air, and magnesia.

Property	Steel	Slag	Air	Magnesia
ρ $(\mathrm{kg/m^3})$	$8580 - 0.883T$	2600	1.225	3580
$C_p(\mathrm{J/(kg{\cdot}K)})$	1200	628	1006.93	937.86
TC $(\mathrm{w/(m{\cdot}K)})$	35	1.1	0.0242	55
μ $(\mathrm{kg/(m{\cdot}s)})$	0.0064	0.09	1.7894×10^{-5}	---

Table 2. Heat losses in the simulation.

Wall	Heat Loss
Bottom	$1400\ \mathrm{w/m^2}$
Back and front	$3200\ \mathrm{w/m^2}$
Right and left	$3800\ \mathrm{J/(kg{\cdot}K)}$
Control flow devices	$1750\ \mathrm{J/(kg{\cdot}K)}$

2.2. Mathematical Model Equations

The mathematical model is based on the Navier-Stokes equations for incompressible flows. The model solves simultaneously the following continuity equations and momentum conservation equations:

$$\frac{\partial \rho}{\partial t} + \frac{\partial}{\partial \mathrm{x}_i}(\rho V_i) = 0 \tag{1}$$

$$\frac{\partial}{\partial \mathrm{t}}(\rho \mathrm{V_i}) + \frac{\partial}{\partial \mathrm{x_i}}(\rho \mathrm{V_i V_j}) = -\frac{\partial \mathrm{P}}{\partial \mathrm{x_i}} + \frac{\partial}{\partial \mathrm{x}}\left[\mu_{\mathrm{eff}}\left(\frac{\partial \mathrm{V_i}}{\partial \mathrm{x_j}} + \frac{\partial \mathrm{V_j}}{\partial \mathrm{x_i}}\right)\right] + \rho\beta\Delta\mathrm{Tg} \tag{2}$$

where ρ is the fluid density. V is the fluid velocity, P is the pressure, μ_{eff} is the effective viscosity given by $\mu_{eff} = \mu + \mu_t$, with μ the fluid viscosity and μ_t the turbulent viscosity, β is the coefficient of volumetric thermal expansion, T is the temperature, and g is the gravity acceleration.

2.2.1. The Standard *k*-ε Realizable Turbulence Model

The realizable *k*-ε proposed by Shih et al. [46] model contains a new formulation for the turbulent viscosity and the dissipation rate ε.

$$\mu_\mathrm{t} = \rho \mathrm{C}_\mu \frac{\mathrm{k}^2}{\varepsilon} \tag{3}$$

where C_μ is no longer a constant.

This model is more accurate for flows involving rotation. Boundary layers under strong adverse pressure gradients, separation, and recirculation.

The equations that describe the transport of the turbulent energy k and dissipation rate ε are given by:

$$\frac{\partial}{\partial t}(\rho k) + \frac{\partial}{\partial x_j}(\rho k j u_j) = \frac{\partial}{\partial x_i}\left[\left(\mu + \frac{\mu_t}{\sigma_k}\right)\frac{\partial k}{\partial x_j}\right] + G_k + G_b - \rho\varepsilon - Y_M + S_k \quad (4)$$

$$\frac{\partial}{\partial t}(\rho\varepsilon) + \frac{\partial}{\partial x_i}(\rho\varepsilon u_i) = \frac{\partial}{\partial x_j}\left[\left(\mu + \frac{\mu_t}{\sigma_\varepsilon}\right)\frac{\partial \varepsilon}{\partial x_j}\right] + \rho C_1 S_\varepsilon - \rho C_2 \frac{\varepsilon^2}{k + \sqrt{\nu\varepsilon}} + C_{1\varepsilon}\frac{\varepsilon}{k} C_{3\varepsilon} G_b + S_\varepsilon \quad (5)$$

In this equation G_k represents the generation of turbulence kinetic energy due to the mean velocity gradients. G_b is the generation of turbulence kinetic energy due to buoyancy Y_M represents the contribution of the fluctuating dilatation in compressible turbulence to the overall dissipation rate, and C_2, $C_{1\varepsilon}$ are constants, σ_k and σ_ε are the turbulent Prandtl numbers. S_k and S_ε are user-defined source terms.

2.2.2. The Lagrangian Discrete Phase Model

The Lagrangian model [47] solves a transport equation for each inclusion as it travels inside the flow field by integrating the force balance acting on the particle. The force balance is as follows:

$$\frac{du_p}{dt} = F_d(V - u_p) + F_B + F_G + F_{VM} + F_{PG} + F_S \quad (6)$$

The drag force per unit particle mass $F_d(V - u_p)$ tends to induce the inclusion to follow the steel flow trajectory. The buoyant (F_B) and gravity forces (F_G), act only in the vertical direction, inducing ascending or descending moves. The term (F_S) corresponds to the Saffman force, which promotes radial and lifting effects. The virtual mass force (F_{VM}) quantifies the required force to accelerate the fluid around the inclusions. The last force in Equation (6) is the gradient force (F_{PG}) generated by the pressure differences from one point to another.

2.3. Numerical Procedure

The simulations are transient following the next sequence: the isothermal case requires simulating 300 s using the implicit formulation and then 60 s using the explicit formulation using 0.01 s as the time step size to achieve the quasi-steady state. For the non-isothermal case, the base was the previously described isothermal case using a time step of 0.005, turning on the temperature. Reaching the quasi-steady state in the explicit formulation for the non-isothermal conditions after the 1920s. The simulation convergence criterion requires residuals smaller than 10^{-4}. All the images and calculations for the isothermal and non-isothermal cases were taken once the simulations achieved the quasi-steady state.

The geometries and dimensions of the scaled one-third model of the tundish and the flow control devices are in Figures 1 and 2. The computational grid shown in Figure 3 consists of 1,500,000 structured cells. The discretization of the governing equations uses the finite volume technique through the commercial CFD code. The non-linear momentum equations were linearized using the implicit approach, and the discretization requires the Second Order Upwind scheme. The pressure interpolations use the PRESTO scheme and the PISO algorithm for the pressure-velocity coupling. The volume of fluid (VOF) [47] method models the multiphase steel-slag-air system.

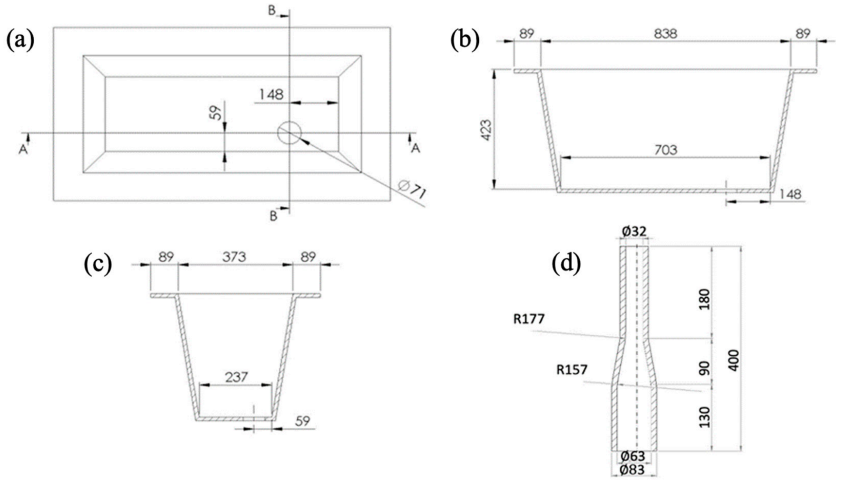

Figure 1. Geometry of the one-third scaled tundish and its flow control devices (mm). (**a**) Upper view; (**b**) frontal view; (**c**) lateral view; and (**d**) ladle shroud.

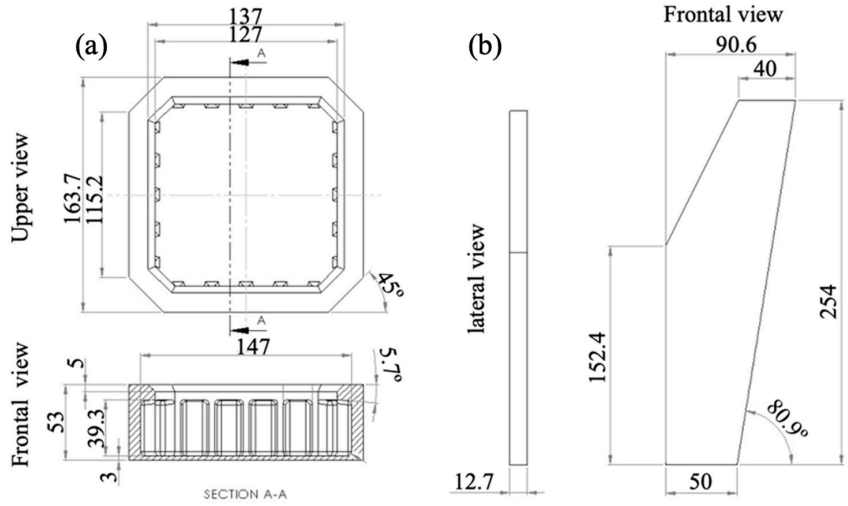

Figure 2. Geometry and dimensions of the one-third scaled (**a**) turbulence inhibitor and (**b**) vortex killer.

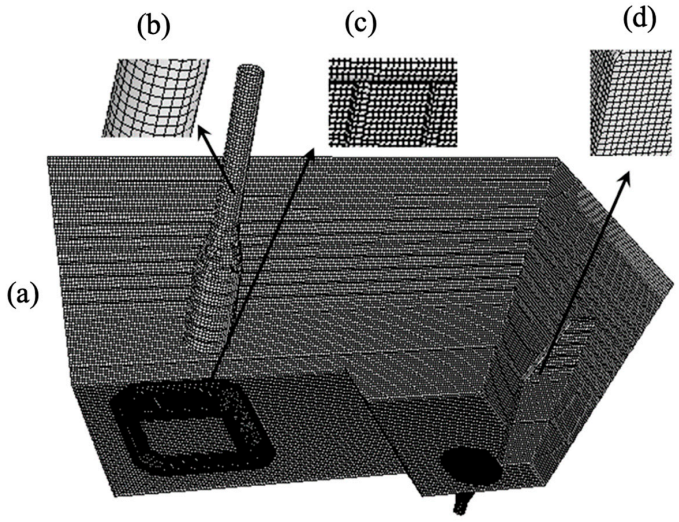

Figure 3. Tundish mesh: (**a**) general view, close up for the (**b**) ladle shroud, (**c**) turbulence inhibitor, and (**d**) vortex killer.

2.4. Physical Model

Physical modeling is a powerful tool for understanding and studying the fluid dynamics occurring inside industrial tundishes, with the advantage of being low-cost. In water physical modeling, the most common scale condition is the Froude similarity criterion, where the ratio between inertial and gravitational forces in the model (m) and prototype (p) must be equal to:

$$\left(\frac{VL\rho}{\mu}\right)_m = \left(\frac{VL\rho}{\mu}\right)_p \tag{7}$$

V and L are the characteristic velocity and length, and ρ is the fluid density. The Froude similarity criterion provides relationships between the variables in the scaled water model and the prototype isothermal tundish. With these relationships, if the variable values are known in the water model, the prototype variable values can be predicted. Some of these relationships, for example, for the length, volumetric flow rate, volume, velocity, and time, are:

$$\begin{aligned} (L)_m &= \lambda (L)_p \\ (Q)_m &= \lambda^{5/2} (Q)_p \\ (Vol)_m &= \lambda^3 (Vol)_p \\ (V)_m &= \sqrt{\lambda}\, (V)_p \\ (t)_m &= \sqrt{\lambda}\, (t)_p \end{aligned} \tag{8}$$

where λ is the scale factor.

Experimental water modeling was carried out on a 1/3 scaled model from the prototype, obeying the Froude criterion. The scaled tundish walls, the turbulence inhibitor, and the vortex killer were built of transparent 12-mm-thick plastic. The scaled ladle shroud and the tundish outlet were made with acrylic block. The working fluid was water at room temperature under isothermal conditions. The tundish was collocated on a metallic structure over a water pit, which has an immersed water pump to transport water through a vertical pipe until the entry of the ladle shroud. The entry flow rate was regulated using a flowmeter, and the tundish model bath level was controlled using a slide gate. Once the scaled model was set, the model was left working for at least 5 min to achieve the steady state of the fluid dynamics, and at this point, the experiments started. A red dye tracer was used to analyze the fluid dynamics of the model; the dye was injected at the top of the ladle shroud, and the dye dispersion movement was recorded with a video camara to make its posterior image analysis.

3. Results and Discussion

3.1. Mathematical Model Validation

Frames from a recorded video of an impulse injection tracer are used to study and analyze the fluid dynamics inside this water model under isothermal conditions. At the same time, predictions of the impulse injection tracer behavior by mathematical modeling are obtained considering again isothermal conditions in a full-scale model. Figure 4 shows the results of tracer behavior for the physical modeling at three representative times (3, 22, and 35 s) and their corresponding times for the mathematical model (5.2, 38, and 61 s) following the equation $(t)_m = \sqrt{\lambda}\, (t)_p$. Figure 4a,b show that the tracer does not enter the tundish homogenously, having a faster entry for the right side. Once the tracer impacts the turbulence inhibitor, it moves upward until it reaches the bath level. Later, it shows two preferential streams: the first moves to the right side, crashing with the lateral tundish wall to continue a descending movement (see Figure 4c,d); the second stream tracer remains moving parallel to the top surface and starts to fall at the half distance between the ladle shroud entry and the right lateral tundish wall; at the same time, another small tracer stream moves close to the tundish floor (see Figure 4e,f). According to the previous results,

it can be considered that the physical and the mathematical models have a good agreement, and consequently, the mathematical model is validated.

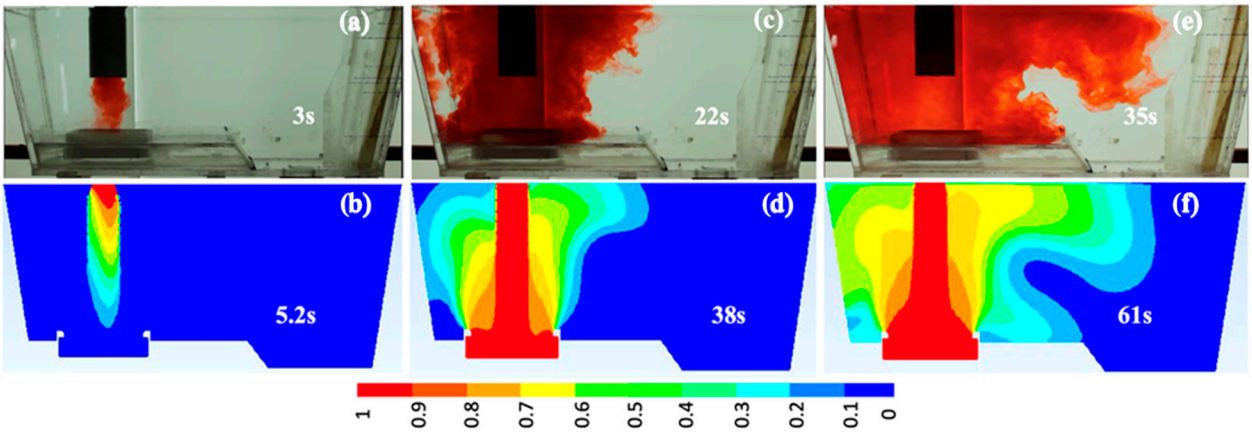

Figure 4. Comparison of the tracer behavior between the 1:3 scale water model (**a**,**c**,**e**) and the full-scale mathematical model (**b**,**d**,**f**).

To demonstrate if a scaled mathematical model can accurately predict the flow patterns and volume fractions as a full-scale model, a 1:3 mathematical model was also simulated. Since the full-scale mathematical model is validated, the following comparison will be made between only the mathematical results: Figure 5a,b exhibits the velocity vector fields in a longitudinal plane at the ladle shroud entry axis. The velocity range is from 0 to 0.023 for the reduced scale case and from 0 to 0.04 m/s, satisfying the expected relationship $(V)_m = \sqrt{\lambda}\,(V)_p$. The similarities between both cases are evident, showing a flow recirculation on the left side of the ladle shroud, a short circuit on the right side, and a second recirculation between the short-circuit position and the tundish floor. Consequently, both mathematical results predict qualitatively the same flow patterns. Nevertheless, it is crucial to verify if the quantifiable parameters also agree. Then, Figure 5c contains the RTD curves for both cases, and Table 3 has the piston, mixed, and dead volume fraction percentages and the non-dimensional residence time for both cases. The same tendency of both curves is visible in Figure 5c. The residence time for the scaled case is 222 s and 372 s for the full-scale case, which satisfy the relation $(t)_m = \sqrt{\lambda}\,(t)_p$ with a difference of 3.7%. The reported values in Table 3 are close for both cases, with a maximum difference of 4% for the mixed volume fraction. Therefore, the above-discussed results demonstrate that the scaled and full-scale models predict the same flow patterns, volume fractions, and residence time, with less than 4% differences following the Froude criteria. Consequently, both mathematical models are equally validated, and either can reasonably well predict the flow patterns of the physical model. Since the current mesh quality and mathematical model predict with good agreement the fluid dynamics of the physical model, mesh sensitivity analysis can be avoided. The present research considers a full-scale model for further analysis since the simulation will include the temperature variable.

Table 3. Volume fraction percentages for the scaled and non-scaled models.

Scale	V_P/V	V_M/V	V_d/V	θ
1:3	46	40	14	0.9
1:1	50	38	12	0.92

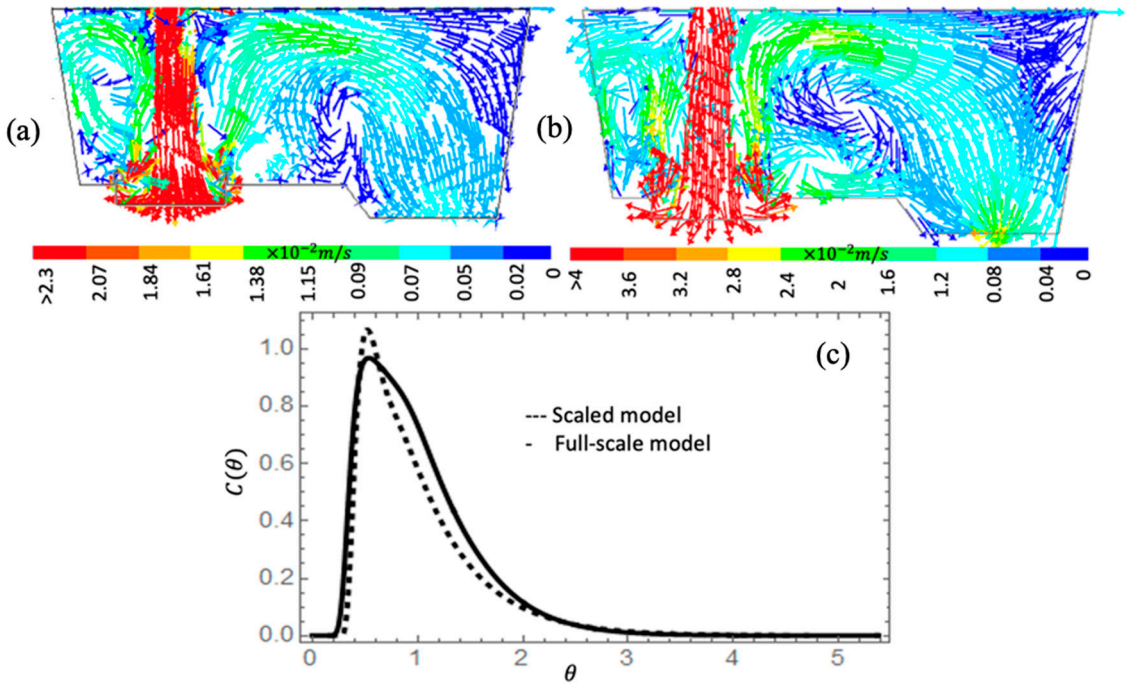

Figure 5. Fixed velocity vectors for (**a**) scaled tundish, (**b**) full-scale tundish, and (**c**) RTD curves for both cases.

3.2. Comparison between Isothermal and Non-Isothermal Cases

To establish the effect of the temperature on the tundish flow patterns, Figure 6 shows tracer concentration contours for three representative times to contrast the tracer behavior for the isothermal (Figure 6a–c) and non-isothermal (Figure 6d–f) cases. Figure 6a,d shows that the tracer behaves similarly in the entry zone for both cases, noting that the flow on the upper right side of the tundish presents a slightly longer trajectory for the non-isothermal case. However, comparing Figure 6b,c, and Figure 6e,f, the tracer shows significant differences in its flow behavior at the top tundish since, for the non-isothermal case, the flow tends to move near the bath level for a longer distance, while for the isothermal case, the tracer presents the same stream with a descending trajectory. Looking for a deeper analysis of the flow patterns, Figure 7 shows the fixed velocity vector fields in three planes: a longitudinal plane at the center of the ladle shroud, a longitudinal plane at the exit, and a horizontal plane at the bath level position.

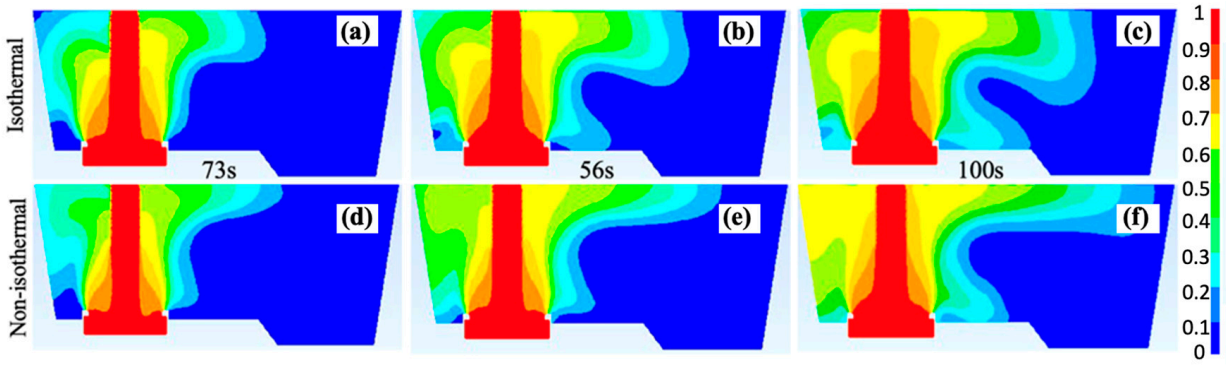

Figure 6. Tracer concentration contours at the central symmetrical plane of the ladle shroud for the isothermal (**a**–**c**) and non-isothermal (**d**–**f**) cases.

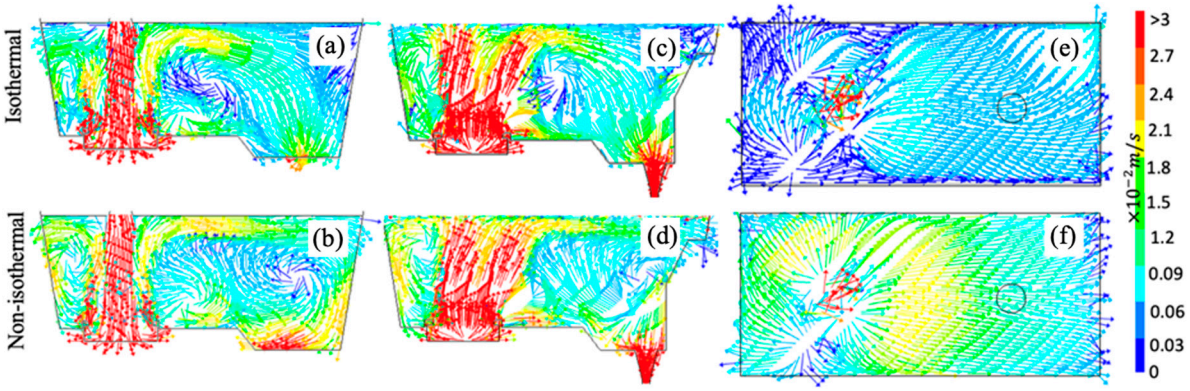

Figure 7. Fixed velocity vector fields in three planes: (**a**,**b**) center of the ladle shroud, (**c**,**d**) center of the exit, and (**e**,**f**) bath level position.

These figures show substantial differences between both cases. For example, the short-circuit previously mentioned in the isothermal case disappears in the non-isothermal case, and the recirculation observed on the right side of the ladle shroud remains in both cases but with different positions and intensities. Also, the non-isothermal case increases the velocity magnitudes for all the planes, being more evident at the bath-level plane. To explain the detected velocity increment, we need the Maxwell-Boltzmann velocity distribution function, which is:

$$f(V)d^3V = \left(\frac{m}{2\,\pi\,k_B\,T}\right)^{3/2} Exp\left[-\frac{m\,V^2}{2\,k_B\,T}\right]d^3V \tag{9}$$

where k_B is the Boltzmann constant, m is the mass particle, T is the temperature, and $f(V)$ is a probability distribution function. The function $f(v)$ indicates the probability of finding a particle with a velocity between V and $V + dV$. Spherical coordinates will be used to find the expression that lets us calculate its value:

$$f(V_x,\ V_y,\ V_z)dV_xdV_ydV_z = f(V_x,\ V_y,\ V_z)V^2dV\ sin\theta d\theta d\varphi \tag{10}$$

Then, after its integration, the Equation (9) becomes:

$$f(V) = \left(\frac{m}{2\,\pi\,k_B\,T}\right)^{1/2} V^2 Exp\left[-\frac{m\,V}{2\,k_B\,T}\right] \tag{11}$$

By choosing two arbitrary temperatures, $T_2 > T_1$, and plotting their corresponding $f(v)$ function in Figure 8, it is possible to understand the effect of the temperature on the velocity distribution function. This figure demonstrates that for the higher temperature T_2, the curve flattens out, the maximum value of the curve diminishes, the maximum value shifts to the left, and the curve becomes narrower in contrast with the curve of T_1. The behavior of this probability distribution function indicates that flows with higher temperatures will have a range of higher velocities. This asseveration applies for the non-isothermal simulation, which will induce that the fluid dynamics present velocity variations because of temperature gradients, being, on average, faster for the hot streams and slower for the cold ones; such velocity variations will not be present in the isothermal case since there are no temperature gradients. Following this analysis and associating velocity increments observed in the non-isothermal case with the previous discussion, it is necessary to study the temperature gradients in the tundish. Figure 9 shows temperature and buoyancy magnitude forces contours. This figure shows that higher temperatures exist in the entry zone and along the bath level. The high velocities at the entry are because of the entry jet. Compared with the isothermal case, the velocity increment observed at the bath level follows the Maxwell-Boltzmann velocity distribution function explanation.

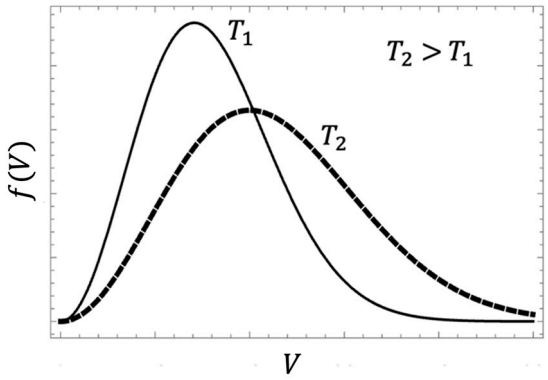

Figure 8. Maxwell–Boltzmann distribution function for two arbitrary temperatures.

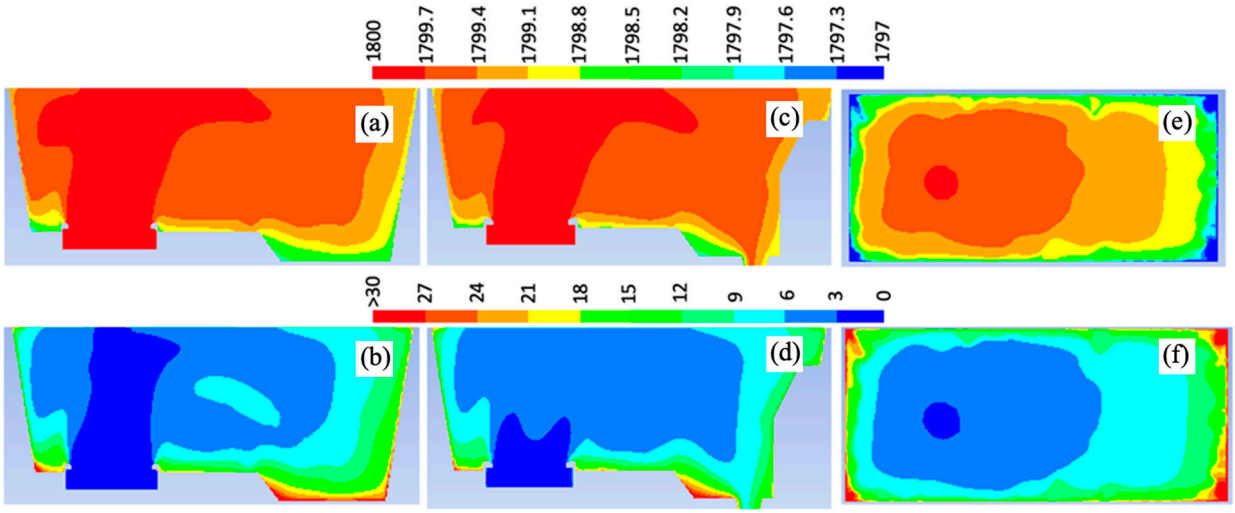

Figure 9. Temperature contours (K) and buoyancy forces (N) at three planes (**a**,**b**) center of the ladle shroud, (**c**,**d**) center of the exit, and (**e**,**f**) bath level position.

Although the Maxwell-Boltzmann velocity distribution function explains velocity magnitude variations between isothermal and non-isothermal models, it cannot explain why the short-circuit disappears under non-isothermal conditions. The buoyancy and inertial forces are studied since these forces are associated with the parameters of temperature and velocity, respectively, to analyze this point.

The buoyancy force depends on temperature variations inside the tundish, and consequently, it only applies to the non-isothermal case and is given by:

$$F_B = \rho\, g\, L^3 \beta\, \nabla T \tag{12}$$

where β is the thermal fluid expansion that arises due to the differences in the fluid density inside the tundish as follows:

$$\beta = -\frac{1}{\rho_{ref}} \left(\frac{\partial \rho}{\partial T} \right)_p = 1.27 \times 10^{-4} K^{-1} \tag{13}$$

Then, given the strong dependency of the buoyancy force on the temperature gradients, the zones that exhibit higher temperature gradients will produce higher buoyancy force values. The results indicate that the main effect of the buoyancy forces occurs in zones near the walls, being less significant in the rest of the tundish, especially at the entry zone. Furthermore, inertial force is another essential force to consider acting in the flow. The inertial force magnitude $F_i = \rho\, V^2 L^2$ is in Figure 10, Figure 10a–c for the isothermal case, and Figure 10d–f for the non-isothermal case. As expected, these figures reflect that

inertial force magnitudes are meaningful throughout the entire tundish. However, the non-isothermal case has more zones where the inertial forces act with higher values than the isothermal case for all the shown planes, especially at the bath level.

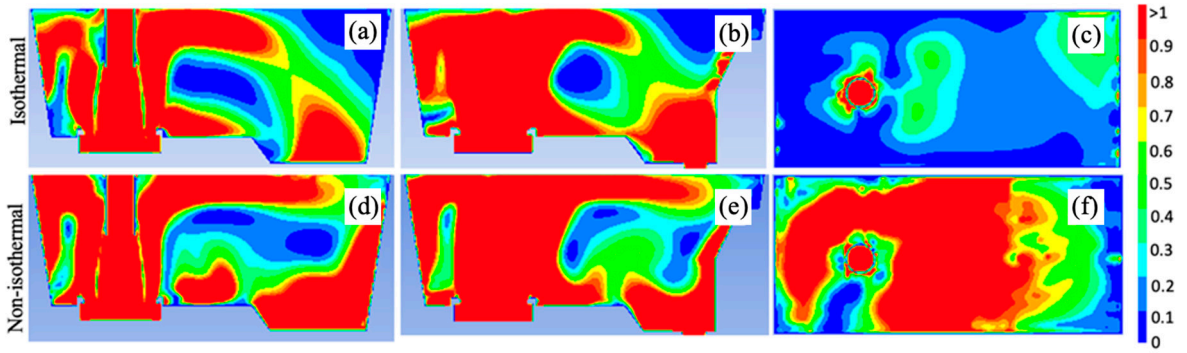

Figure 10. Inertial force magnitude (N) at three planes, for the isothermal and non-isothermal cases, (**a**,**d**) center of the ladle shroud, (**b**,**e**) center of the exit, and (**c**,**f**) bath level position.

To observe which of the two analyzed forces dominates each region of the tundish, the Richardson number (Ri) will be employed. This number defines the ratio of buoyancy force to inertial force as follows:

$$\mathrm{Ri} = \frac{gL\beta\Delta T}{V^2} \tag{14}$$

Then, if Ri tends to zero, the inertial force is predominant over the buoyancy force, and it is opposite when the ratio is higher than one. Figure 11 shows the contours of the Ri values for the non-isothermal case in the three analyzed planes. The results show that the inertial force dominates over the buoyancy force in the entry zone, around the ladle shroud at the bath level, and very close to the outlet; in contrast, buoyancy force dominates in the detected recirculation zones (points ① and ②) and dead flow zones (points ③, ④, and ⑤). It is crucial to notice that zones where Ri tends to zero correspond to zones with less appreciable flow pattern changes between isothermal and non-isothermal cases.

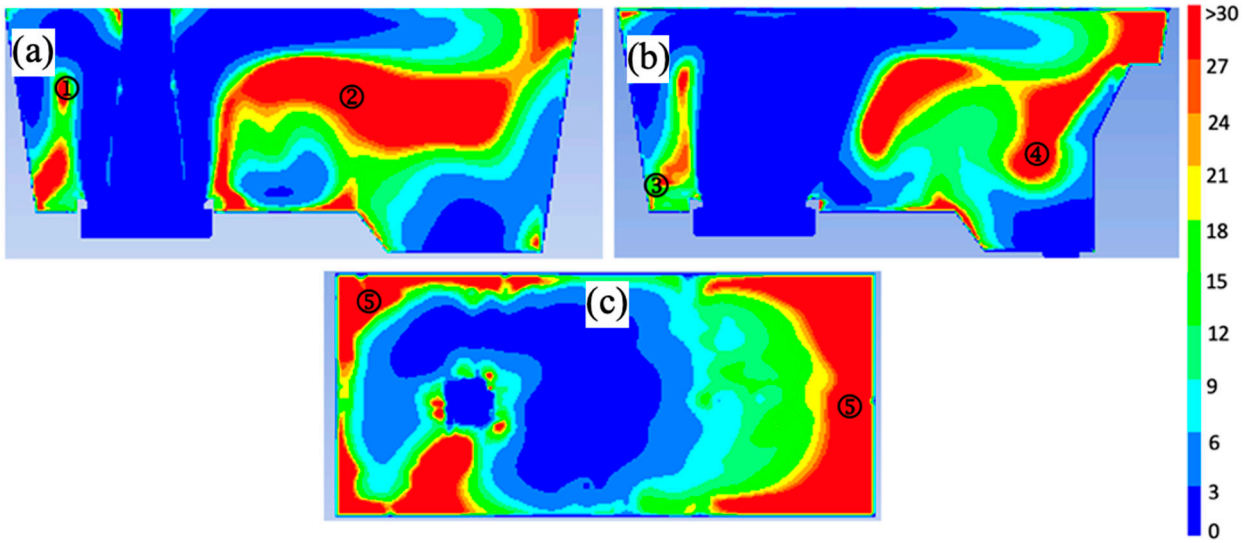

Figure 11. Richardson number magnitude at three planes. (**a**) center of the ladle shroud; (**b**) center of the exit nozzle; and (**c**) upper view of the tundish at the bath level.

Considering the above discussion from Figures 6–10, the flow variations observed between the isothermal and non-isothermal cases have now been supported. The upward stream flow reaching the bath surface from the turbulence inhibitor has a higher temperature than the rest of the bulk flow. This hotter flow must follow the Maxwell-Boltzmann

velocity distribution function, which, together with the buoyancy forces acting upwards below this stream, induces the following changes: (1) at the left ladle shroud side, the recirculation moves upward with an increment in the flow velocity around it; (2) at the right ladle shroud side, the mainstream, moving parallel to the bath level towards the right tundish wall and traveling near the metal-slag interphase, has higher velocity, which reaches a longer distance than in the isothermal case. The second implication forces the short circuit to disappear, moving the recirculation below it toward the right tundish side. These changes are even when the temperature variations inside the tundish are as modest as 3 K. Until this point, the fluid dynamic changes between both cases have been analyzed and explained; however, it is necessary to determine their effect on variables such as volume fractions and inclusion removal rate quantitatively.

Figure 12 shows the RTD curves for both cases. The figure reveals that the curves present similarities in the first appearance of the tracer, θ_{min}, and when the tracer's maximum concentration occurs, θ_{max}. However, it is noticeable that the non-isothermal curve is the highest and slightly thinner than the isothermal one. These differences are quantifiable by the volume fraction calculation presented in Table 4.

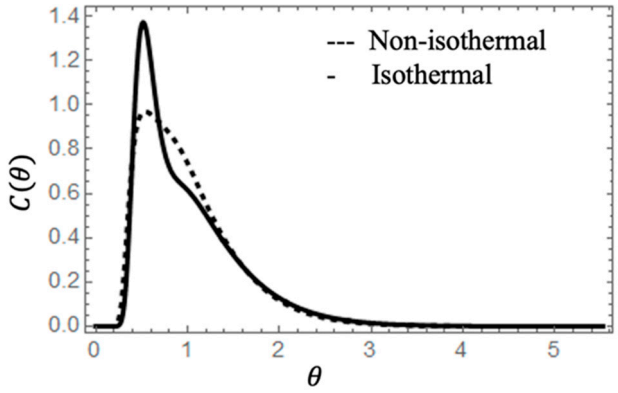

Figure 12. RTDs for isothermal and non-isothermal cases.

Table 4. Volume fraction percentages for the isothermal and non-isothermal models.

Case	V_P/V	V_M/V	V_d/V	θ
Isothermal	50	38	12	0.93
Non-isothermal	46	39	15	0.91

The results indicate that the volume fraction percentages are similar with a flow moving mainly as a mixed flow. In addition, there is an increment in the piston flow of 1%, a decrement in the mixed flow of 4%, an increment in the dead volume of 3%, and a decrement in the non-dimensional residence time of 2.1% for the non-isothermal case concerning the isothermal case.

To study if the temperature variable affects the behavior of the inclusions inside the tundish, first the changes in the number of removed inclusions were analyzed for both cases. To do this, for a single inclusion size, 2000 inclusions were fed at the ladle shroud entry as an impulse once the fluid dynamics acquired the quasi-steady state condition, and through the Lagrangian model, which uses the current flow patterns, the trajectories of the 2000 inclusions were calculated using the removal boundary condition previously indicated. As a result, the Lagrangian model indicates the number of inclusions that were removed in the steel-slag interphase and the number of inclusions that have reached the tundish exit. With this information, the inclusion removal percentage was calculated using Equation (15):

$$inclusion\ removal\ percentage = \frac{amount\ of\ removed\ inclusions}{2000} \times 100 \quad (15)$$

This procedure was the same for each of the inclusion sizes. Figure 13a presents the inclusion removal percentage calculated by the DPM for the inclusion sizes considered in this work, for isothermal and non-isothermal cases. The results show that the removed inclusions in a range of 1 to 40 µm are at least 35% of the fed inclusions, and the inclusion removal percentage, for both cases, is almost 100% for inclusions bigger than 130 µm. The non-isothermal case presents an increment of 5% in the inclusion removal percentages in comparison with the isothermal case for inclusions ranging from 1 to 60 µm; this was the most significant difference between the results for both cases.

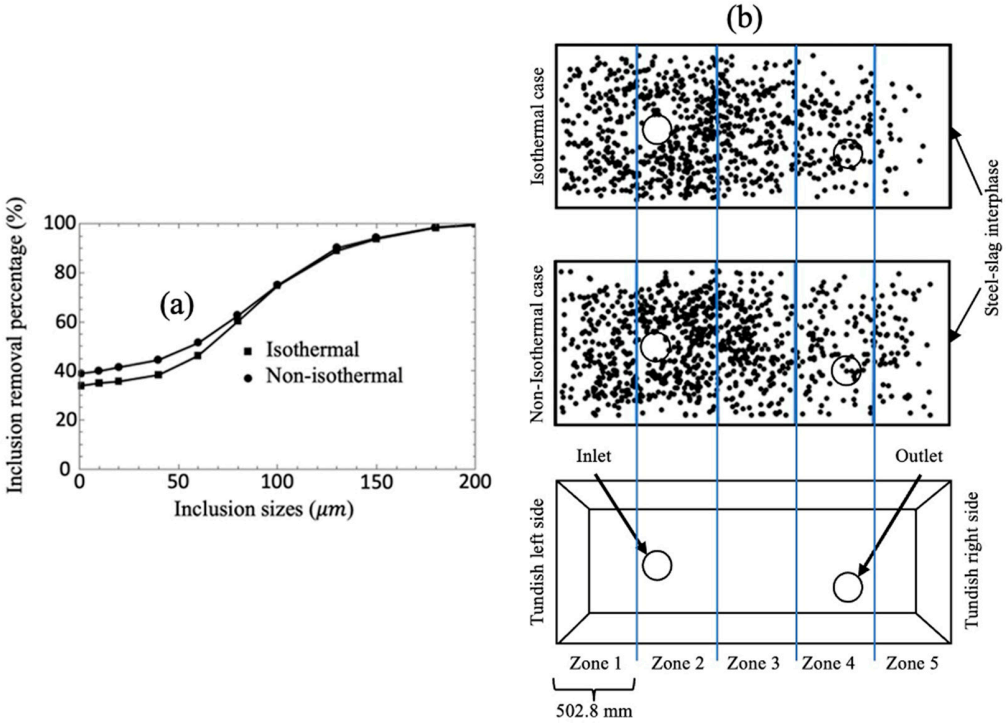

Figure 13. (**a**) Inclusion removal percentages for many inclusion sizes. (**b**) Sample of the removed inclusion distribution at the steel-slag interphase using 40 µm.

Previously, it has been demonstrated that the temperature barely affects the global tendency of the removal of inclusion percentages; however, it could be possible that the temperature affects the way inclusions are distributed when they are removed. To obtain the exact position where each inclusion was removed at the steel-slag interphase, a user-defined function (UDF) was employed within the CFD software. Figure 13b shows the removed inclusion distribution at the steel-slag interphase for an inclusion size of 40 µm in both cases. The results indicate that both removed inclusion distributions are quite similar, highlighting some characteristics: Most of the inclusions are removed around the ladle shroud zone, and towards the outlet position, the number of removed inclusions decreases. This behavior is attributed to the fluid dynamics induced by the turbulence inhibitor and the absence of more flow control devices between the turbulence inhibitor and the tundish outlet. These results apparently indicate that the temperature does not influence the removed inclusion distribution at the steel-slag interphase. In order to do a comparison between the number of inclusions and their removed position for each inclusion size, the steel-slag interface was divided into five zones of equal length. Subsequently, the removed inclusion positions were determined for each inclusion size, and the number of removed inclusions at each zone was calculated as a percentage for isothermal and non-isothermal cases. Figure 14 shows the removed inclusion percentage for each inclusion size calculated for the zones indicated in Figure 13b for isothermal and non-isothermal cases. The results of Figure 14 indicate that the removed inclusion distribution is similar for all the inclusion sizes regarding the non-isothermal or isothermal conditions. Therefore, the flow velocity increment in the

non-isothermal case and the short circuit in the isothermal case do not significantly impact the inclusion removal rate and its removed distribution at the bath level.

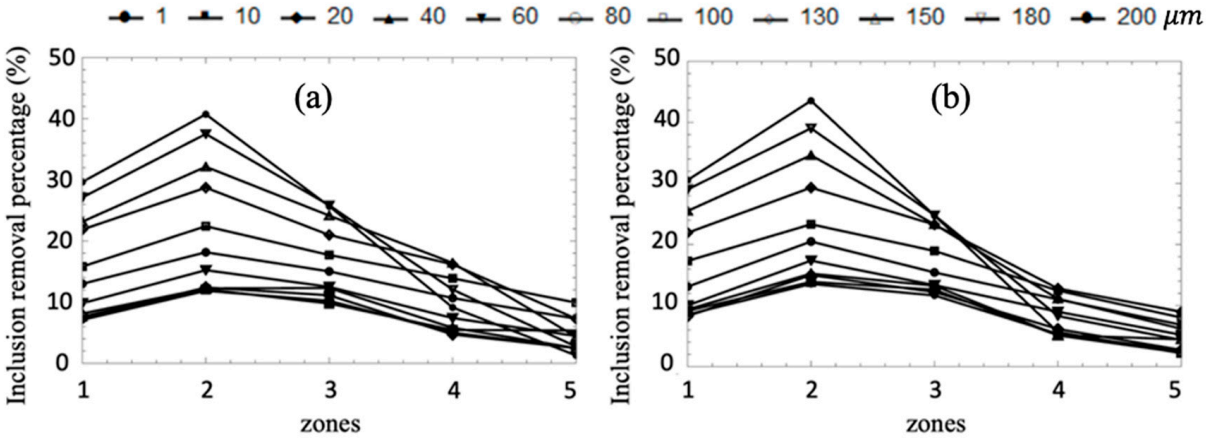

Figure 14. Inclusion removal percentages by zones in the tundish bath level (**a**) isothermal case, (**b**) non-isothermal case.

4. Conclusions

This work investigates the temperature effect on the fluid patterns and inclusion removal rates in a continuous casting tundish using mathematical simulation. From the previously discussed results, the following conclusions are drawn:

(1) The quantification of the differences between the results of 1:3 scaled and full-scale models, which have a maximum difference of 4% on the volume fractions percent and residence time, demonstrate that scaled and full-scale models can be used reliably to predict the flow patterns of an isothermal physical model following the Froude criteria.

(2) Temperature gradients inside the tundish induce variations in the flow velocity magnitude; if the stream has a higher temperature than its surrounding flow, its velocity will increase because of the Maxwell-Boltzmann velocity distribution function; this supports why hot streams, e.g., at the bath level, under non-isothermal conditions, have bigger velocity magnitudes than the same streams but under isothermal conditions.

(3) The quantification of the ratio between inertial and buoyancy forces demonstrates that inertial forces dominate over buoyancy forces at the entry zone because turbulence inhibitors strongly control the fluid dynamics in such an area. In contrast, buoyancy forces take more relevance than inertial forces in the recirculation and dead flow zones, inducing noticeable changes in the fluid dynamics between isothermal and non-isothermal cases far from the entry zone.

(4) Although the temperature induces substantial fluid dynamic changes between the analyzed cases, this variable does not significantly impact the volume fraction percentages or the mean residence time results, and it only increases the inclusion removal percentage by 5% for the non-isothermal case.

(5) The effect of the temperature on the flow patterns is not significant when the flow control devices strongly rule the fluid dynamics; nevertheless, when the flow control devices effects are not dominant, the temperature takes substantial importance because of the buoyancy forces and the increment of flow velocity because the Maxwell Boltzmann velocity distribution function changes the fluid dynamics in comparison with the obtained from the isothermal conditions. Consequently, isothermal simulations can accurately describe the flow behavior in tundishes, where flow control devices control the fluid dynamics. However, the simulation of tundishes without control devices or with a weak fluid dynamic dependence on the control devices requires non-isothermal simulations.

5. Future Work

Since temperature variance could depend on the turbulence model, and as a consequence, these differences can produce density variations and affect the flow, a further analysis of the differences between isothermal and non-isothermal models must be conducted, considering different turbulence models and many tundish designs.

Author Contributions: Conceptualization, R.M.D. and J.d.J.B.; methodology, E.G.; software, E.G. and S.G.-H.; validation, R.M.D. and E.G.; formal analysis, E.G. and S.G.-H.; investigation, E.G.; resources, E.G. and R.M.D.; data curation, E.G.; writing—original draft preparation, E.G. and S.G.-H.; writing—review and editing, E.G., S.G.-H. and J.d.J.B.; visualization, E.G.; supervision, R.M.D.; project administration, E.G. All authors have read and agreed to the published version of the manuscript.

Funding: This research received no external funding.

Data Availability Statement: Data are contained within the article.

Acknowledgments: The authors thank TecNM-ITM and SNI institutions for their permanent support of the Academic Research Group.

Conflicts of Interest: The authors declare no conflicts of interest.

Nomenclature

ρ	Fluid density (kg/m^3)
C_p	Specific heat (J/(kg K))
TC	Thermal conductivity (w/(m K))
μ	Dynamic viscosity (kg/(m s))
V	Fluid velocity (m/s)
u_p	Particle velocity (m/s)
P	Pressure (Pa)
t	Time (s)
T	Temperature (K)
μ_{eff}	Effective Viscosity (kg/(m s))
g	Gravity acceleration (m/s^2)
β	Coefficient of volumetric thermal expansion (K^{-1})
ε	Turbulent dissipation rate (m^2/s^3)
k	Kinetic energy (m^2/s^2)
G_k	Generation of turbulent kinetic energy due to the mean velocity gradients
G_b	Generation of turbulent kinetic energy due to buoyancy
Y_M	Contribution of the fluctuating dilatation in compressible turbulence to the dissipation rate
$F_d(V\text{-}u_p)$	Drag force per unit mass (N/kg)
F_B, F_G, F_S, F_{VM}, F_{PG}	The buoyant, gravitational, Saffman, virtual mass, and gradient force per unit mass (N/kg)
$C_{1\varepsilon}$, $C_{2\varepsilon}$, $C_{3\varepsilon}$	Model constants
σ_k, σ_ϵ	Turbulent Prandtl numbers
S_k, S_ϵ	User-defined source terms
L	Characteristic length (m)
λ	Scale factor
V_P/V	Piston volume fraction
V_M/V	Mixed volume fraction
V_d/V	Dead volume fraction
θ	Non-dimensional residence time
k_b	Boltzmann constant
K	Kelvin
Ri	Richardson number

References

1. Sheng, D.; Jönsson, P. Effect of Thermal Buoyancy on Fluid Flow and Residence-Time Distribution in a Single-Strand Tundish. *Materials* **2021**, *14*, 1906. [CrossRef] [PubMed]
2. Wang, Q.; Liu, Y.; Huang, A.; Yan, W.; Gu, H.; Li, G. CFD Investigation of Effect of Multi-hole Ceramic Filter on Inclusion Removal in a Two-Strand Tundish. *Metall. Mater. Trans. B* **2020**, *51*, 276–292. [CrossRef]
3. Cwudzinski, A. Physical and mathematical simulation of liquid steel mixing zone in one strand continuous casting tundish. *Int. J. Cast. Met. Res.* **2017**, *30*, 50–60. [CrossRef]
4. Agarwal, R.; Singh, M.K.; Kumar, R.; Ghosh, B.; Pathak, S. Extensive Analysis of Multi Strand Billet Caster Tundish Using Numerical Technique. *J. Mech.* **2019**, *9*, 29–51. [CrossRef]
5. Xing, F.; Zheng, S.; Liu, Z.; Zhu, M. Flow Field, Temperature Field, and Inclusion Removal in a New Induction Heating Tundish with Bent Channels. *Metals* **2019**, *9*, 561. [CrossRef]
6. Ramirez, O.D.; Torres-Alonso, E.; Ramos-Banderas, A.; Villa, S.A.; Bocanegra, C.H.; Martínez, J.T. Thermal and Fluid-Dynamic Optimization of a Five Strand Asymmetric Delta Shaped Billet Caster Tundish. *Steel Res. Int.* **2018**, *89*, 1–10. [CrossRef]
7. Tang, H.; Guo, L.; Wu, G.; Xiao, H.; Yao, H.; Zhang, J. Hydrodynamic Modeling and Mathematical Simulation on Flow Field and Inclusion Removal in a Seven-Strand Continuous Casting Tundish with Channel Type Induction Heating. *Metals* **2018**, *8*, 374. [CrossRef]
8. Neves, L.; Tavares, R. Analysis of the mathematical model of the gas bubbling curtain injection on the bottom and the walls of a continuous casting tundish. *Ironmak. Steelmak.* **2017**, *44*, 559–567. [CrossRef]
9. Sahai, Y. Tundish Technology for Casting Clean Steel: A Review. *Metall. Mater. Trans. B* **2016**, *47*, 2095–2106. [CrossRef]
10. Wang, Q.; Li, B.; Tsukihash, F. Hydrodynamic Problem in Continuous Casting Tundish with Channel Type Induction Heating. *ISIJ Int.* **2014**, *54*, 311–320. [CrossRef]
11. Ni, P.; Jonsson, L.T.I.; Ersson, M.; Jönsson, P.G. Turbulent Flow Phenomena and Ce_2O_3 Behavior during a Steel Teeming Process. *ISIJ Int.* **2013**, *53*, 792–801. [CrossRef]
12. Qu, T.; Liu, C.; Jiang, M.; Zu, L. Numerical Simulation for Effect of Inlet Cooling Rate on Fluid Flow and Temperature Distribution in Tundish. *J. Iron Steel Res. Int.* **2012**, *19*, 12–19. [CrossRef]
13. Ling, H.; Zhang, L. Numerical Simulation of the Growth and Removal of Inclusions in the Molten Steel of a Two-Strand Tundish. *JOM* **2013**, *65*, 1155–1163. [CrossRef]
14. Singh, V.; Ajmani, S.; Pal, A.; Singh, S.; Denys, M. Single strand continuous caster tundish furniture comparison for optimal performance. *Ironmak. Steelmak.* **2012**, *39*, 171–179. [CrossRef]
15. Braun, A.; Warzecha, M.; Pfeifer, H. Numerical and Physical Modeling of Steel Flow in a Two-Strand Tundish for Different Casting Conditions. *Metall. Mater Trans. B* **2010**, *41*, 549–559. [CrossRef]
16. Vargas-Zamora, A.; Morales, R.D.; Díaz-Cruz, M.; Palafox-Ramos, J.; Demedices, L.G. Heat and mass transfer of a convective-stratified flow in a trough type tundish. *Int. J. Heat Mass Transf.* **2003**, *46*, 3029–3039. [CrossRef]
17. Joo, S.; Han, J.; Guthrie, R. Inclusion behavior and heat-transfer phenomena in steelmaking tundish operations: Part II. Mathematical model for liquid steel in tundishes. *Metall. Mater Trans. B* **1993**, *24*, 767–777. [CrossRef]
18. Chakraborty, S.; Sahai, Y. Effect of Varying Ladle Stream Temperature on the Melt Flow and Heat Transfer in Continuous Casting Tundishes. *ISIJ Int.* **1991**, *31*, 960–967. Available online: https://www.jstage.jst.go.jp/article/isijinternational1989/31/9/31_9_960/_pdf (accessed on 4 January 2024). [CrossRef]
19. Miki, Y.; Thomas, B. Modeling of inclusion removal in a tundish. *Metall. Mater. Trans. B* **1999**, *30*, 639–654. [CrossRef]
20. Alizadeh, M.; Edris, H. Prediction of RTD Curves for Non-isotherm steel Melt Flows in Continuous Casting Tundish. In Proceedings of the International Symposium on Liquid Metal Processing and Casting, LMPC, Nancy, France, 2–5 September 2007; pp. 167–172.
21. Sun, H.; Yan, B.; Zhang, J. Effect of Thermal Buoyancy Force on the Flow, Temperature Distribution and Residence Time Distribution of Molten Steel in the Slab Casting Tundish. In *CFD Modeling and Simulation in Materials Processing*; The Minerals, Metals, & Materials Society: Pittsburgh, PA, USA, 2012; pp. 327–334. [CrossRef]
22. Chatterjee, S.; Chattopadhyay, K. Transient steel quality under non-isothermal conditions in a multi-strand billet caster tundish: Part II. Effect of a flow-control device. *Ironmak. Steelmak.* **2016**, *44*, 413–420. [CrossRef]
23. Zhu, M.; Peng, S.; Jiang, K.; Luo, J.; Zhong, Y.; Tang, P. Fluid Flow and Heat Transfer Behaviors under Non-Isothermal Conditions in a Four-Strand Tundish. *Metals* **2022**, *12*, 840. [CrossRef]
24. Morales, R.; Lopez-Ramirez, S.; Palafox-Ramos, J.; Zacharias, D. Mathematical simulation of effects of flow control devices and buoyancy forces on molten steel flow and evolution of output temperatures in tundish. *Ironmak. Steelmak.* **2001**, *28*, 33–43. [CrossRef]
25. Chattopadhyay, K.; Isac, M.; Guthrie, R. Modelling of Non-isothermal Melt Flows in a Four Strand Delta Shaped Billet Caster Tundish Validated by Water Model Experiments. *ISIJ Int.* **2012**, *52*, 2026–2035. [CrossRef]
26. de Sousa, J.; Barros, E.; Marcondes, F.; de Castro, J. Modeling and computational simulation of fluid flow, heat transfer and inclusions trajectories in a tundish of a steel continuous casting machine. *J. Mater. Res. Technol.* **2019**, *8*, 4209–4220. [CrossRef]
27. Neumann, S.; Asad, A.; Schwarze, R. Numerical Simulation of an Industrial-Scale Prototypical Steel Melt Tundish Considering Flow Control and Cleaning Strategies. *Adv. Eng. Mater.* **2020**, *22*, 1900658. [CrossRef]

28. Mishra, R.; Mazumdar, D. Numerical Analysis of Turbulence Inhibitor Toward Inclusion Separation Efficiency in Tundish. *Indian Inst. Met.* **2019**, *72*, 889–989. [CrossRef]
29. Gutiérrez, E.; Garcia-Hernández, S.; de Barreto, J. Mathematical Analysis of the Touching Inclusions Parameters at the Tundish Free Surface to Predict More Realistic Inclusion Removal Rates. *Steel Res. Int.* **2019**, *90*, 1900328. [CrossRef]
30. Gutiérrez, E.; Garcia-Hernández, S.; de Barreto, J. Mathematical Modeling of Inclusions Deposition at the Upper Tundish Nozzle and the Submerged Entry Nozzle. *Steel Res. Int.* **2016**, *87*, 1406–1416. [CrossRef]
31. Gutiérrez, E.; Garcia-Hernández, S.; de Barreto, J. Mathematical Analysis of the Dynamic Effects on the Deposition of Alumina Inclusions inside the Upper Tundish Nozzle. *ISIJ Int.* **2016**, *56*, 1394–1403. [CrossRef]
32. Lei, H.; Zhao, Y.; Geng, D. Mathematical Model for Cluster-Inclusion's Collision-Growth in Inclusion Cloud at Continuous Casting Mold. *ISIJ Int.* **2014**, *54*, 1629–1637. [CrossRef]
33. Liu, Z.; Li, B.; Jiang, M. Transient Asymmetric Flow and Bubble Transport Inside a Slab Continuous-Casting Mold. *Metall. Mater. Trans. B* **2014**, *45*, 675–697. [CrossRef]
34. Liu, Z.; Li, B.; Jiang, M.; Tsukihashi, F. Euler-Euler-Lagrangian Modeling for Two-Phase Flow and Particle Transport in Continuous Casting Mold. *ISIJ Int.* **2014**, *54*, 1314–1323. [CrossRef]
35. Takahashi, K.; Ando, M.; Ishii, T. Model of Gas Flow Through Porous Refractory Applied to an Upper Tundish Nozzle. *ISIJ Int.* **2014**, *54*, 304–405. [CrossRef]
36. He, Z.; Zhou, K.; Liu, S.; Xiong, W.; Li, B. Numerical Modeling of the Fluid Flow in Continuous Casting Tundish with Different Control Devices. *Abstract Appl. Anal.* **2013**, *2013*, 984894. [CrossRef]
37. Seshadri, V.; da Silva, C.; da Silva, I.; Junior, E. A Physical Modelling Study Of Inclusion Removal In Tundish Using Inert Gas Curtain. *Tecnol. Metal. Mater. Min.* **2012**, *9*, 22–29. [CrossRef]
38. Long, M.; Zuo, X.; Zhang, L.; Chen, D. Kinetic Modeling on Nozzle Clogging During Steel Billet Continuous Casting. *ISIJ Int.* **2010**, *50*, 712–720. [CrossRef]
39. Zhong, L.; Li, L.; Wang, B.; Zhang, L.; Zhu, L.; Zhang, Q. Fluid flow behaviour in slab continuous casting tundish with different configurations of gas bubbling curtain. *Ironmak. Steelmak.* **2008**, *35*, 436–440. [CrossRef]
40. Ramos-Banderas, A.; Morales, R.D.; de Barreto, J.; Solorio-Diaz, G. Modelling Study of Inclusions Removal by Bubble Flotation in the Tundish. *Steel Res. Int.* **2006**, *77*, 325–335. [CrossRef]
41. Yuan, Q.; Thomas, B.; Vanka, S. Study of transient flow and particle transport in continuous steel caster molds: Part II. Particle transport. *Metall. Mater. Trans. B* **2004**, *35B*, 703–714. [CrossRef]
42. Vermeulen, Y.; Coletti, B.; Blanpain, B.; Wollants, P.; Vleugels, J. Material Evaluation to Prevent Nozzle Clogging during Continuous Casting of Al Killed Steels. *ISIJ Int.* **2002**, *42*, 1234–1240. [CrossRef]
43. Zhang, L.; Taniguchi, S.; Cai, K. Fluid flow and inclusion removal in continuous casting tundish. *Metall. Mater. Trans. B* **2000**, *31*, 253–266. [CrossRef]
44. Sasai, K.; Mizukami, Y. Reaction Mechanism between Alumina Graphite Immersion Nozzle and Low Carbon Steel. *ISIJ Int.* **1994**, *34*, 802–809. [CrossRef]
45. Fukuda, Y.; Ueshima, Y.; Mizoguchi, S. Mechanism of Alumina Deposition on Alumina Graphite Immersion Nozzle in Continuous Caster. *ISIJ Int.* **1992**, *32*, 164–168. [CrossRef]
46. Shih, T.; Liou, W.; Shabbir, A.; Yang, Z.; Zhu, J.A. A new k-ϵ eddy viscosity model for high reynolds number turbulent flows. *Comput. Fluids* **1995**, *24*, 227–238. [CrossRef]
47. ANSYS Inc. *FLUENT 12.0, User's Guide*; Centerra Resource Park: Cavendish Court, Lebanon, 2009. Available online: https://www.afs.enea.it/project/neptunius/docs/fluent/html/ug/main_pre.htm (accessed on 4 January 2024).